ELSEVIER

Journal of Biomechanics 39 (2006) 2064–2073

JOURNAL OF BIOMECHANICS

www.elsevier.com/locate/jbiomech
www.JBiomech.com

Multiphase hemodynamic simulation of pulsatile flow in a coronary artery ☆

Jonghwun Jung[a], Robert W. Lyczkowski[b,*], Chandrakant B. Panchal[b], Ahmed Hassanein[a]

[a]*Argonne National Laboratory, Energy Technology Division, Argonne, IL 60439-4815, USA*
[b]*Argonne National Laboratory, Energy Systems Division, 9700 S. Cass Avenue, Argonne, IL 60439-4815, USA*

Accepted 10 June 2005

Abstract

A multiphase transient non-Newtonian three-dimensional (3-D) computational fluid dynamics (CFD) simulation has been performed for pulsatile hemodynamics in an idealized curved section of a human coronary artery. We present the first prediction, to the authors' knowledge, of particulate buildup on the inside curvature using the multiphase theory of dense suspension hemodynamics. In this study, the particulates are red blood cells (RBCs). The location of RBC buildup on the inside curvature correlates with lower wall shear stress (WSS) relative to the outside curvature. These predictions provide insight into how blood-borne particulates interact with artery walls and hence, have relevance for understanding atherogenesis since clinical observations show that atherosclerotic plaques generally form on the inside curvatures of arteries.

The buildup of RBCs on the inside curvature is driven by the secondary flow and higher residence times. The higher viscosity in the central portion of the curved vessel tends to block their flow, causing them to migrate preferentially through the boundary layer. The reason for this is the nearly neutrally buoyant nature of the dense two-phase hemodynamic flow.

The two-phase non-Newtonian viscosity model predicts greater shear thinning than the single-phase non-Newtonian model. Consequently, the secondary flow induced in the curvature is weaker. The waveforms for computed hemodynamic parameters, such as hematocrit, WSS, and viscosity, follow the prescribed inlet velocity waveforms. The lower oscillatory WSS produced on the inside curvature has implications for understanding thickening of the intimal layer.

Keywords: Multiphase; Non-Newtonian; Coronary artery; Computational fluid dynamics; Wall shear stress

1. Introduction

The development of atherosclerosis in humans begins by the adhesion of monocytes to the endothelium (Hajjar and Nicholson, 1995; Fung, 1997; Ku, 1997; Nichols and O'Rourke, 1998; Stary, 1999; Berger and Jou, 2000; Berne and Levy, 2001; Taylor and Draney, 2004). The trigger for the response is not yet known in spite of decades of study (Steinman, 2002). Atherosclerosis is localized near side branches and on the inner curvature of arteries (Thubrikar and Robicsek, 1995). This has been known since the time of Rudolph Virchow (1821–1902) (Bonert et al., 2003), a pioneering Prussian physician and pathologist. The hemodynamic stresses and forces play important roles in the initial stages of cardiovascular disease. This observation is also not new having been proposed over a century ago as reported by Malek et al., (1999). The biomechanical environment in the cardiovascular system almost certainly plays a key

☆This manuscript has been created by the University of Chicago as Operator of Argonne National Laboratory ("Argonne") under Contract no. W-31-109-Eng-38 with the US Department of Energy. The US Government retains for itself, and others acting on behalf, a paid-up, nonexclusive, irrevocable worldwide license and said article to reproduce, prepare derivative works, distribute copies to the public, and perform publicly and display publicly, by or on behalf of the Government.

*Corresponding author. Tel.: +1 630 252 5923; fax: +1 630 252 5910.
E-mail address: rlyczkowski@anl.gov (R.W. Lyczkowski).

0021-9290/$ - see front matter © 2005 Elsevier Ltd. All rights reserved.
doi:10.1016/j.jbiomech.2005.06.023

role in arterial disease, including atherogenesis and in the diagnosis and treatment of patients with cardiovascular disease (Steinman et al., 2003). Shear stress can activate platelets and the biomechanical factors are important in monocyte rolling and adhesion.

One of the earliest reviews of atheroma (Caro et al., 1969) claims its association with arterial blood mechanics. There are several hypotheses as to the cause of and progression of atherosclerosis. These include (1) high hemodynamic wall shear stress (WSS), (2) low WSS, (3) high arterial wall stress [more accurately referred to as tensile or hoop stress (Higdon et al., 1976)], (4) high WSS gradients (WSSG), and (5) damage to the endothelium. These critical issues have subsequently been the subject of continuing discussion in the literature for several decades (Nerem, 1993; Thubrikar and Robicsek, 1995; Davies et al., 1997; Wootton and Ku 1999; Malek et al., 1999; Steinman, 2002; Bonert et al., 2003).

Using their single-phase computational fluid dynamics (CFD) model, Qiu and Tarbell (2000) predicted low WSS on the inside curvature of an idealized model of a left coronary artery (LCA). Zeng et al. (2003) failed to find a consistent correlation between their single-phase WSS CFD computations and curvature in a realistic reconstruction of a right coronary artery (RCA).

Steinman (2002) concluded that the lack of progress in the last three decades is because most studies, until recently, have been *retrospective* using idealized or averaged hemodynamic models rather than being *prospective* using local measured hemodynamic indices and correlated in a noninvasive manner using CFD models. Steinman et al. (2003) stressed that the specific causative link between biomechanical factors and arterial pathogenesis remains to be identified in part because of the substantial complexity of the highly unsteady, three-dimensional (3-D) biomechanical arterial environment. The confirmation of various hypotheses is lacking and the exact cause eludes investigators. We feel that the major reason for this lingering situation is the use of single-phase CFD in the analyses. What has been missing is the application of *multiphase theory*. Like Taylor and Draney (2004), we are humbled by the explorations of distinguished predecessors in the field of fluid dynamics of the human cardiovascular system.

In this study, it is shown that for an idealized model of a human coronary artery, particulates buildup on the inside curvature. This prediction may serve as a first step in understanding atherogenesis since it is consistent with clinical observations that atherosclerotic plaque generally forms preferentially on the inside curvatures of arteries (Thubrikar and Robicsek, 1995; Davies, 1995; Qiu and Tarbell, 2000; Zeng et al., 2003). This signal study is a significant first step in the systematic analysis of multiphase cardiovascular hemodynamics and the authors know of no such previous effort.

2. Methods

2.1. Multiphase hemodynamic model

A multiphase non-Newtonian 3-D CFD model for describing the hemodynamics in vascular vessels is developed. It uses the principles of mass, momentum, and energy conservation for each phase. This approach, based on the generalization of the well-known Navier–Stokes equations, is similar to that of Anderson and Jackson (1967) and Gidaspow (1994). The principle difference compared with a single-phase model is the appearance of the volume fraction for each phase, as well as mechanisms for the exchange of mass, momentum, and energy between the phases. Gidaspow (1994) gives a detailed description of multiphase flow. The governing equations and constitutive relations represent the unique confluence of over 30 years of single-phase cardiovascular modeling (Steinman, 2002) and the nearly 30 years of multiphase theory and CFD modeling as reviewed by Gidaspow (1994). This approach builds upon and extends the work of Lyczkowski and Wang (1992) and Ding et al. (1993, 1995), who analyzed dense negatively and neutrally buoyant two-phase liquid–solids suspension flows.

In the two-phase non-Newtonian hemodynamic model, the continuous phase is plasma, which is a Newtonian fluid (Lightfoot, 1974). The predominant particulate phase suspended in the plasma comprises the red blood cells (RBCs) having a hematocrit, H, or volume fraction, $\varepsilon_{\mathrm{RBC}}$, in the normal range of 35–50%. Platelets and white blood cells (of which monocytes are a member) constitute an aggregate volume fraction less than 1%. In this paper, RBCs are modeled more realistically since they control the blood rheology. This is important when modeling monocyte adhesion.

The continuity equation for each phase (k = plasma, RBCs) is given by

$$\frac{\partial(\rho_k \varepsilon_k)}{\partial t} + \nabla \cdot (\rho_k \varepsilon_k \vec{v}_k) = 0, \tag{1}$$

where ρ is density, ε is volume fraction, t is time, and $\vec{v}$ is velocity. The sum of the volume fractions for each phase must sum to one:

$$\sum_{k=1}^{\mathrm{np}} \varepsilon_k = 1.0, \tag{2}$$

where np is the total number of phases.

The momentum equation for each phase (k = plasma, RBCs) is given by

$$\frac{\partial(\rho_k \varepsilon_k \vec{v}_k)}{\partial t} + \nabla \cdot (\rho_k \varepsilon_k \vec{v}_k \vec{v}_k) = \varepsilon_k \rho_k \vec{g} - \varepsilon_k \nabla p + \nabla \cdot \varepsilon_k \bar{\bar{\tau}}_k + \sum_{l \neq k} \beta_{kl} (\vec{v}_l - \vec{v}_k) + \vec{F}_k. \tag{3}$$

The terms of the RHS of Eq. (3) represent gravity $\vec{g}$, shear stress $\bar{\bar{\tau}}$, pressure p, drag force between the carrier fluid and particulates, and external forces $\vec{F}$, such as virtual mass, rotational and shear lift, electric, and magnetic. In the drag force, k and l represent plasma or RBCs, and β_{kl} are the interphase momentum exchange coefficients.

In order to effect closure for Eqs. (1)–(3), we require several constitutive relations.

The blood mixture density, ρ_{mix}, is given by the sum of the volume fraction weighted plasma and RBCs densities neglecting the minor blood-borne constituents as

$$\rho_{\text{mix}} = \varepsilon_{\text{plasma}}\rho_{\text{plasma}} + \varepsilon_{\text{RBC}}\rho_{\text{RBC}}. \tag{4}$$

We used a mixture density of $1080\,\text{kg/m}^3$ (Gijsen et al., 1999a), an inlet hematocrit of 45% (Dill and Costill, 1974), and a plasma density of $1000\,\text{kg/m}^3$.

The stress tensor for each phase is given by the Newtonian form as follows (Gidaspow, 1994):

$$\bar{\bar{\tau}}_k = 2\mu_k\bar{\bar{D}}_k - \tfrac{2}{3}\mu_k\,\text{tr}(\bar{\bar{D}}_k). \tag{5}$$

The deformation tensor, $\bar{\bar{D}}_k$, is given by

$$\bar{\bar{D}}_k = \tfrac{1}{2}[\nabla\vec{v}_k + (\nabla\vec{v}_k)^{\text{T}}]. \tag{6}$$

The rheological model for blood viscosity is a key factor in the simulation of hemodynamic flows. Ding et al. (1995), showed that the non-Newtonian shear-thinning model is very important to describe neutrally buoyant dense suspension flow at high solids volume fractions. The experimental rheological data of Wojnarowski (2001) and Brooks et al. (1970) for human blood depends not only upon the shear rate, but also upon the hematocrit, H. The dimensionless relative mixture viscosity, η, was correlated from these data using an extension of the Carreau–Yasuda viscosity model (Bird et al., 1987):

$$\eta = \frac{\varepsilon_{\text{RBC}}\mu_{\text{RBC}} + \varepsilon_{\text{plasma}}\mu_{\text{plasma}}}{\mu_{\text{plasma}}} = m[1 + (\lambda\dot{\gamma})^2]^{(n-1)/2}, \tag{7}$$

where m, λ, and n are parameters and $\dot{\gamma}$ is the shear rate (1/s) (Fig. 1). The time constant, λ, is given by 0.110 s, the same as used by Gijsen et al. (1999b). The plasma viscosity, μ_{plasma}, is treated as a Newtonian fluid (Lightfoot, 1974) having a viscosity of $0.001\,\text{kg/m s}$ (1 cp). The two parameters n and m in Eq. (7) are correlated as functions of hematocrit, $H = \varepsilon_{\text{RBC}}$, using a polynomial given by

$$n = 0.8092\varepsilon_{\text{RBC}}^3 - 0.8246\varepsilon_{\text{RBC}}^2 - 0.3503\varepsilon_{\text{RBC}} + 1$$

and

$$m = 122.28\varepsilon_{\text{RBC}}^3 - 51.213\varepsilon_{\text{RBC}}^2 + 16.305\varepsilon_{\text{RBC}} + 1. \tag{8}$$

The 45% hematocrit, H, represented by the solid line (Fig. 1) is in good agreement with Wojnarowski's (2001) rheological data. The dimensionless relative mixture viscosity increases with hematocrit, H, and decreases with increasing dimensionless shear rate, displaying shear-thinning behavior (Fig. 1). As the hematocrit goes to zero, Eq. (7) reduces to the Newtonian plasma viscosity.

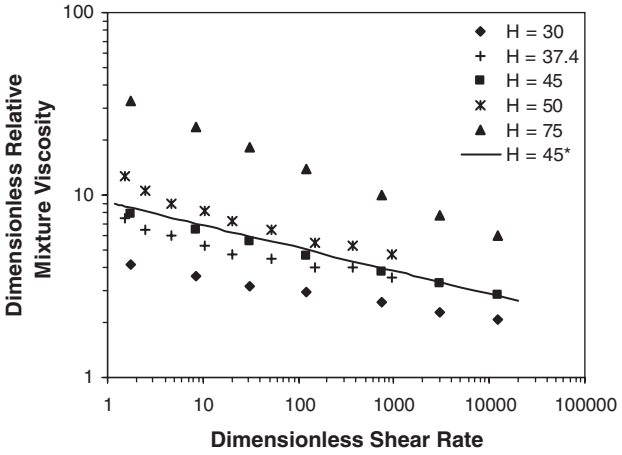

Fig. 1. Dimensionless relative blood viscosity, η, Eq. (7), as a function of dimensionless shear rate, $1 + \lambda\dot{\gamma}^2$ and percent hematocrit, H. Data sources: Wojnarowski (2001), $H = 30$, 45, 75 and Brooks et al. (1970), $H = 37.4$, 50. The solid line represents a 45% hematocrit computed from Eq. (7).

As a particulate moves through a viscous fluid, there is exerted a resistance to its motion caused by the interphase drag. The interphase momentum exchange coefficient, β_{kl}, between plasma and RBCs is given by the Schiller and Naumann model (Fluent, Inc., 2003a) as

$$\beta_{kl} = \frac{3}{4}C_{\text{d}}\frac{\rho_{\text{plasma}}\varepsilon_{\text{plasma}}\varepsilon_{\text{RBC}}|\vec{v}_{\text{plasma}} - \vec{v}_{\text{RBC}}|}{d_{\text{RBC}}\phi}. \tag{9}$$

The drag coefficient, C_{d}, given by

$$C_{\text{d}} = \frac{24}{Re_{\text{p}}}[1 + 0.15\,Re_{\text{p}}^{0.687}] \quad \text{for } Re < 1000, \tag{10}$$

$$C_{\text{d}} = 0.44 \quad \text{for } Re \geqslant 1000, \tag{11}$$

is related to the Reynolds number, Re_{p}, as

$$Re_{\text{p}} = \frac{\rho_{\text{plasma}}d_{\text{RBC}}|\vec{v}_{\text{plasma}} - \vec{v}_{\text{RBC}}|\phi}{\mu_{\text{plasma}}}, \tag{12}$$

where d_{RBC} is the diameter of RBCs and ϕ is the shape factor.

Other external forces acting on each phase consist of the virtual mass and shear lift forces. The virtual mass force in the FLUENT code (Fluent, Inc., 2003a) is given by

$$\vec{F}_{\text{vm},k} = 0.5\varepsilon_m\rho_k\left(\frac{d_k\vec{v}_k}{\text{d}t} - \frac{d_m\vec{v}_m}{\text{d}t}\right)\Bigg|_{k\neq m}$$

$$(\vec{F}_{\text{vm},k} = -\vec{F}_{\text{vm},m}), \tag{13}$$

where

$$\frac{d\vec{v}}{dt} = \frac{\partial \vec{v}}{\partial t} + (\vec{v} \cdot \nabla)\vec{v}. \quad (14)$$

The shear lift force in the FLUENT code is given by

$$\vec{F}_{\text{lift},k} = -0.5\varepsilon_m \rho_k (\vec{v}_k - \vec{v}_m) \times (\nabla \times \vec{v}_k)|_{k \neq m}$$
$$(\vec{F}_{\text{lift},k} = -\vec{F}_{\text{lift},m}). \quad (15)$$

The virtual mass effect occurs when one phase accelerates relative to the other phase. The lift force acts on a particulate phase due to velocity gradients in the primary-phase flow field. Only the virtual mass force was included in our coronary artery simulation.

2.2. Numerical considerations

We used the commercial CFD code FLUENT 6.1 (Fluent, Inc., 2003a), which contains the multiphase 3-D Eulerian–Eulerian model. The numerical solution method uses a finite volume, unstructured mesh, staggered grid arrangement. The scalar variables are located at the cell centers and the vector variables are located at the cell boundaries. The momentum equations are solved using a staggered mesh, while the continuity equations are solved using a donor cell method. The two-phase Eulerian–Eulerian model in the FLUENT code was validated by reanalyzing the neutrally buoyant dense suspension NMR slurry data modeled by Ding et al. (1995) (see webpage of the Journal of Biomechanics: www.elsevier.com/locate/jbiomech). The non-Newtonian shear-thinning viscosity model given by Eq. (7) and the transient inlet phase velocity waveforms for the cardiac cycle were programmed into the FLUENT code as UDF and profile files.

All simulations for the idealized rigid wall coronary artery were carried out using the 3-D computational domain (Fig. 2). The artery is modeled using a uniform diameter, $D = 4.37$ mm (Berne and Levy, 2001; Berthier et al., 2002). The total length of the idealized coronary artery is 0.13 m with a radius of curvature, $R = 4.1515$ cm. The value of (R/a) used here, where a is the artery radius, is 19, approximating a coronograph of an RCA used by Berthier et al. (2002). Straight exit and entry tubes were attached to the idealized curved coronary artery to remove exit effects and to ensure a fully developed velocity profile entering the curved section. A mesh was generated using GAMBIT 2.1 software (Fluent, Inc., 2003b) using the Cooper mesh generation algorithm. Three boundary layer meshes having a total thickness of 0.2 mm were used next to the vessel wall in order to better resolve the shear gradients. The total number of nodes for the mesh was 46,339. Stewart and Lyman (2004) analyzed artery vascular graft compliance mismatch between the proximal and distal coronary arteries for conditions very similar to those used in the study. They found that doubling and quadrupling the number of meshes from 23,798 generated by the GAMBIT software did not significantly affect their results using the single-phase FIDAP CFD code. Therefore, we are confident that the results predicted in this study are accurate and essentially mesh independent.

A pulsatile inlet velocity waveform was used as inlet boundary conditions for both the RBCs and plasma (Fig. 3), based upon the waveform for a right coronary artery from Nichols and O'Rourke (1998). The in vivo pressure waveforms measured in the ascending aorta by Cholley et al. (1995) and Poppas et al. (1997) were used to adjust the timings of the systole, diastole, and total cardiac cycle period. The velocity profiles were maintained uniform across the inlet cross-section. The zero slip velocity boundary condition was employed for both RBCs and plasma. The inlet volume fraction of RBCs

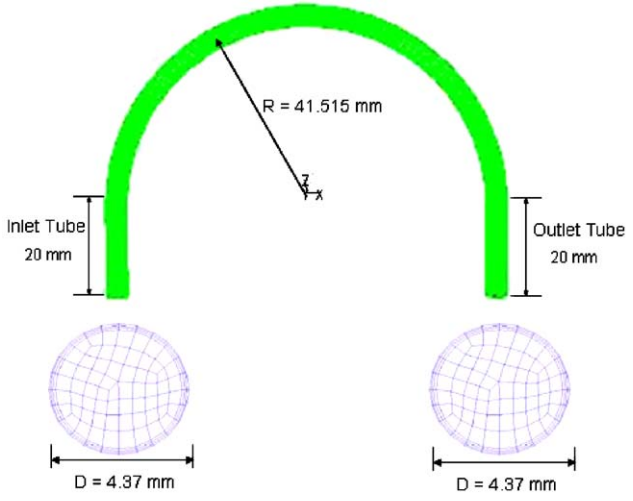

Fig. 2. Three-dimensional computational grid for an idealized curvature coronary artery generated using Cooper mesh generation algorithm using GAMBIT software (Fluent, Inc., 2003b).

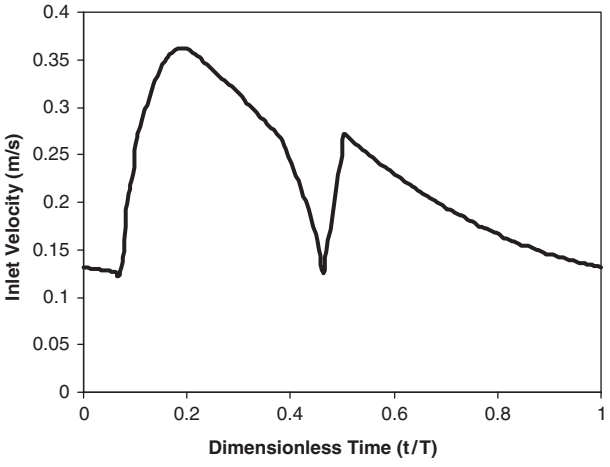

Fig. 3. Pulsatile coronary inlet velocity waveform for RBCs and plasma. Dimensionless time t/T is scaled by the cardiac cycle period, $T = 0.735$ s.

was maintained uniform and steady at 45%. For initial conditions, the RBC volume fraction was set to 45% and both RBC and plasma velocities were set to zero. The exit reference pressure was set to $1.02 \times 10^4\,\mathrm{kg/m\,s^2}$ (75 mmHg) above atmospheric. The maximum residual for convergence was 10^{-3} with a constant time step of 10^{-4} s. The computations were run for three complete cardiac cycles. Data analysis was performed for the third cardiac cycle.

In our CFD simulation, the mean Reynolds number ($Re = \rho_{\mathrm{mix}} U_0 D/\mu_{\mathrm{mix}}$), based on average inlet velocity, $U_0 = 0.22\,\mathrm{m/s}$ and artery diameter, $D = 4.37\,\mathrm{mm}$, is about 230. The Womersley parameter, $\alpha = D/2\sqrt{2\pi/T\,(\rho_{\mathrm{mix}}/\mu_{\mathrm{mix}})}$, where T is the cardiac period $= 0.73$ s, is about 3.12, approximately the same value used by Stewart and Lyman (2004). The Dean number, $Dn = Re/\sqrt{(R/a)}$, used to characterize curved tube flows is about 53. These characteristic hemodynamic parameter values are in good agreement with the results of other single-phase coronary artery simulations (Rappitsch et al., 1997; Gijsen et al., 1999b; Qiu and Tarbell, 2000; Zeng et al., 2003). RBCs were considered as spherical particles with an average diameter of 8 μm and a shape factor, $\phi = 1$. The major objective is to determine the spatial and temporal distributions of RBCs, volume fraction, velocity, viscosity, shear rate, WSS and WSSG during the cardiac cycles.

3. Results

We simulated the two-phase flow of RBCs and plasma in an idealized coronary artery with the non-Newtonian shear-thinning viscosity model (Fig. 1) and the inlet velocity waveform (Fig. 3). The computed RBC volume fractions are found to be highest on the inside radius of curvature (Fig. 4). The color bar shows the range of RBC volume fractions. Secondary flows in the curvature cross section are characterized by two vortices with weak up flow in the center and stronger flow in the boundary layer. The secondary flows weaken during the diastole, resulting in an increase in the RBCs buildup on the inside curvature. By the third cardiac cycle, the ratio of the volume fraction of RBCs in the inside curvature to the initial value is about 1.013.

The secondary flows produced in the center curvature cross section results in unsymmetrical axial velocity contours and profiles (Fig. 5). The axial velocity profile has a maximum shifted towards the outside curvature. Hence the shear rate is higher than on the inside curvature. The RBC viscosity contours and profiles also have a maximum shifted towards the outside curvature (Fig. 6). The RBC viscosity reaches a maximum value of about 0.018 kg/m s (18 cp) at a dimensionless radial position of about 0.1.

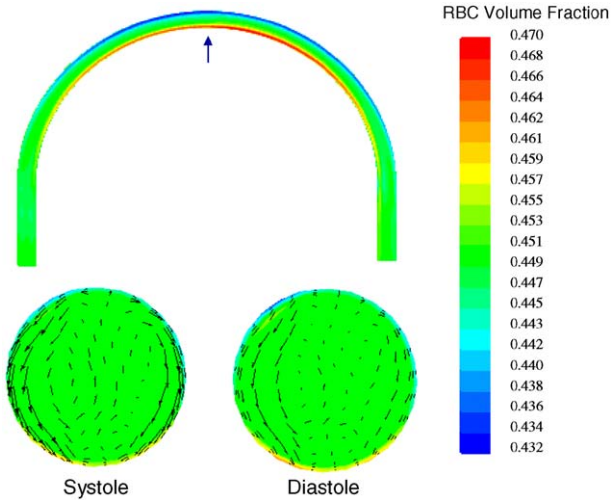

Fig. 4. RBC volume fraction and secondary flow (vector plots) in the third cardiac cycle. The cross sections for the systole (1.61 s) and diastole (2.20 s) are at the center curvature indicated by the arrow. The inside curvature is at the bottom of each cross section and the outside curvature is at the top.

The waveforms for the computed RBC shear rate, viscosity and WSS during the third cardiac cycle follow the prescribed inlet velocity waveforms (Fig. 7). The shear rate suddenly increases at the beginning of the systole, then decreases to nearly zero by the end (Fig. 7A). The shear rate then rises sharply again at the beginning of the diastole followed by a gradual decline. The viscosity waveform follows an inverse process due to the shear-thinning behavior. The RBC viscosity attains a maximum value at the beginning of the diastole. The average RBC shear rate is 350 (1/s) and the average RBC viscosity is 0.0075 kg/m s (7.5 cp) on the inside curvature during the third cardiac cycle and are 520 (1/s) and 0.0063 kg/m s (6.3 cp) on the outside curvature, respectively.

Both RBC WSS waveforms on the inside and outside curvatures follow the inlet velocity waveform, reaching a maximum value of about $2.1\,\mathrm{N/m^2}$ during the diastole (Fig. 7B). The average WSS is $1.065\,\mathrm{N/m^2}$ on the inside curvature and $1.383\,\mathrm{N/m^2}$ on the outside curvature in good agreement with other CFD model simulations (Qiu and Tarbell, 2000; Zeng et al., 2003).

We analyzed axial velocities and WSSs predicted by the single-phase and multiphase non-Newtonian CFD models using the same inlet velocity waveform (Fig. 3). The non-Newtonian viscosity model for single-phase flow is a function of shear rate alone with a hematocrit, H, of 45% (Fig. 1) and a density of $1080\,\mathrm{kg/m^3}$. Compared with the multiphase CFD model, the single-phase CFD model has more unsymmetrical axial velocity contours with the maximum shifted more towards the outside curvature (Fig. 8).

The secondary flow for the multiphase non-Newtonian CFD model simulation is much weaker and the

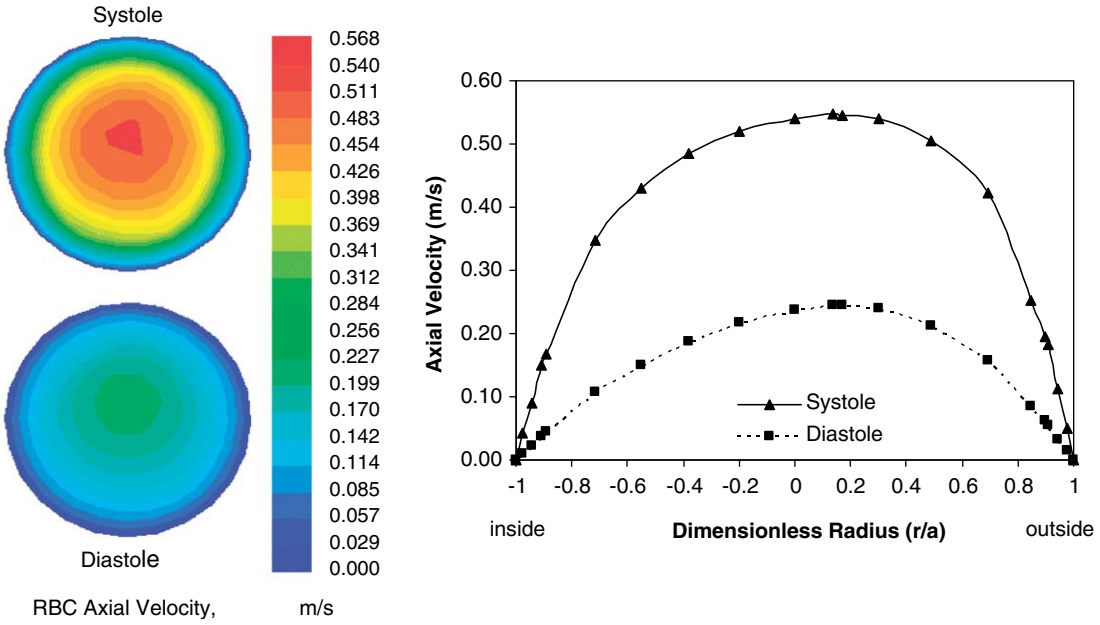

Fig. 5. RBC axial velocity contours and profiles in the cross section location indicated in Fig. 4 (systole = 1.61 s, diastole = 2.20 s, a: artery radius).

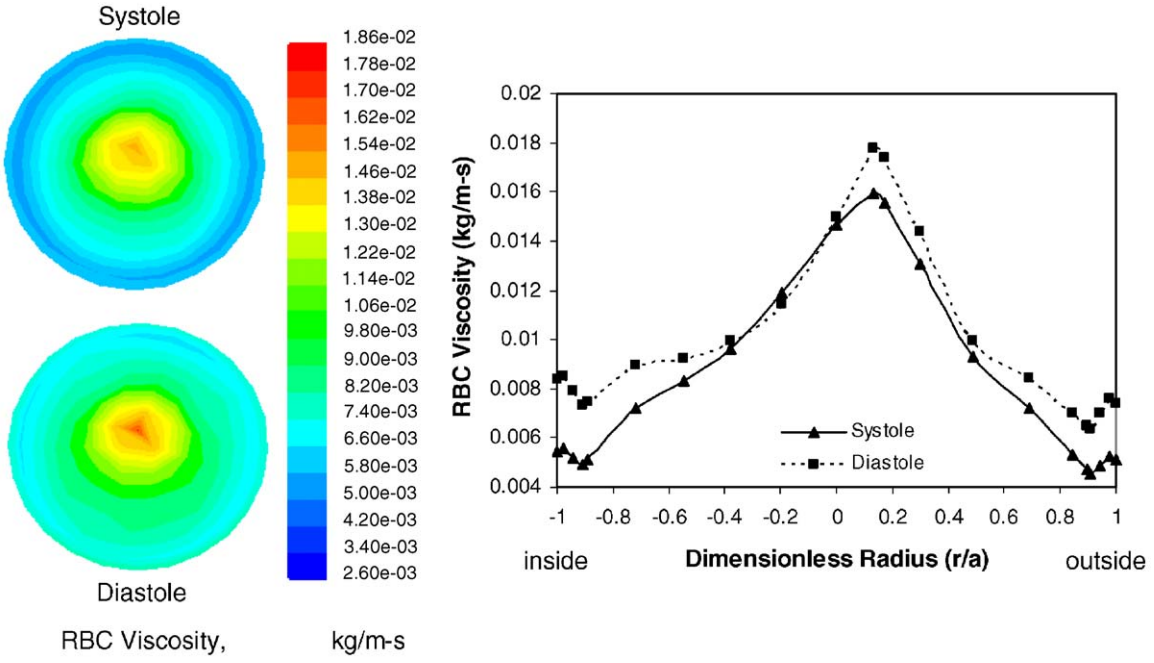

Fig. 6. RBC viscosity contours and profiles in the cross section location indicated in Fig. 4 (systole = 1.61 s, diastole = 2.20 s).

axial velocity profile is flatter in the central region than that for the single-phase non-Newtonian CFD model simulation (Fig. 8). This can be better understood by examining the multiphase and single-phase viscosities and WSSs (Fig. 9).

The mixture viscosity for the multiphase non-Newtonian CFD model is somewhat higher than the single-phase non-Newtonian CFD model on the inside and the outside curvatures (Fig. 9A). Both single-phase and multiphase viscosities are consistently higher on the inside curvature than on the outside curvature. Most of the mixture viscosity for the multiphase non-Newtonian CFD model (Fig. 9A) is due to the RBC viscosity (Fig. 7A). The average of the computed mixture viscosity is roughly 0.0035 kg/m s (3.5 cp).

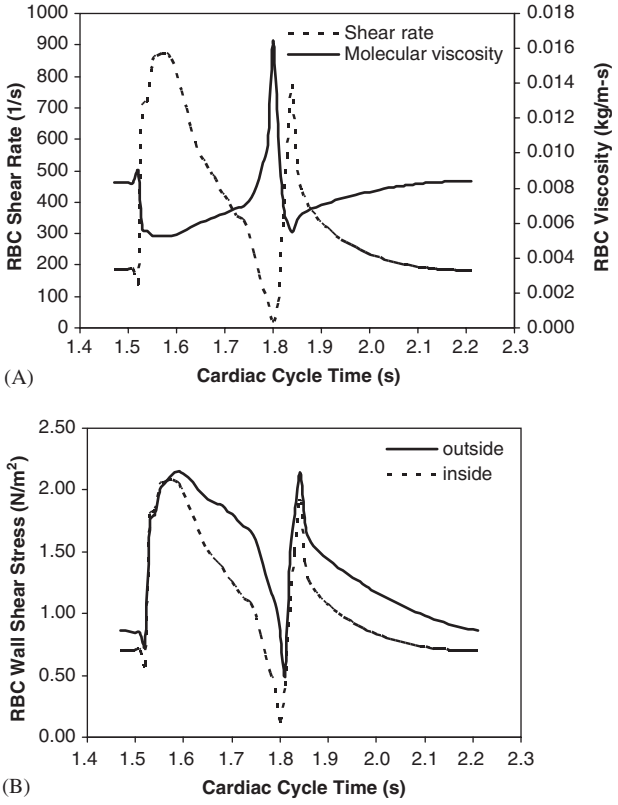

Fig. 7. (A) Computed RBC shear rate and viscosity during the third cardiac cycle time on the inside curvature. (B) Comparison of RBC wall shear stresses on the inside curvature with that on the outside curvature.

The WSS on the inside curvature for the multiphase and single-phase CFD models are similar and lower than on the outside curvature (Fig. 9B). However, the WSS on the outside curvature for the single-phase CFD model is much higher than the multiphase non-Newtonian CFD model (Fig. 9B). This is due primarily to the higher shear rate for the single-phase CFD model caused by its axial velocity shifted more toward the outside curvature than the single-phase CFD model (Fig. 8). Most of mixture WSS for the multiphase non-Newtonian CFD model (Fig. 9B) is due to the RBCs (Fig. 7B).

The multiphase CFD model predicts somewhat higher WSSG near the walls than the single-phase model (Fig. 10). We found that most of the contribution to the WSSG in the multiphase CFD model is due to the RBCs. Therefore, the RBCs play a dominant role in the hemodynamics.

4. Discussion

The multiphase Eulerian–Eulerian transient non-Newtonian 3-D CFD simulation predicts the buildup of particulates on the inside curvature of an idealized model of a coronary artery for the first time to the authors' knowledge. This prediction is only possible using the multiphase Eulerian–Eulerian CFD model of dense suspension hydrodynamics. We found a

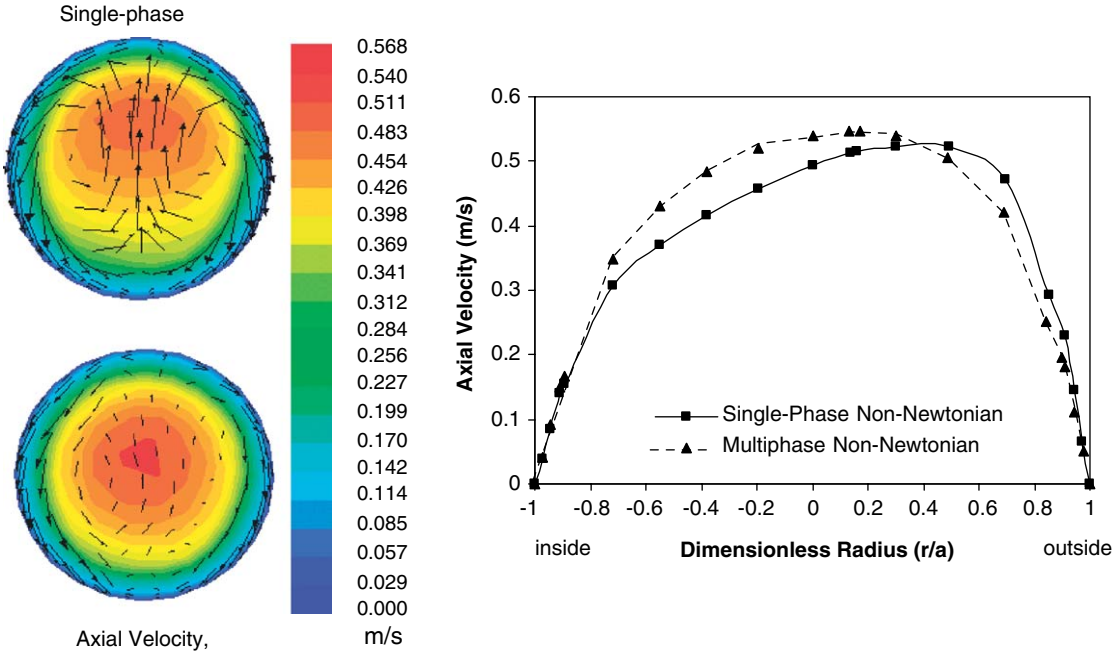

Fig. 8. Comparison of axial velocity contours, profiles and secondary flows for single-phase and multiphase non-Newtonian models at the peak of the third systole, $t = 1.61$ s. The magnitude of vector scale for secondary flow for the single-phase model is one half times higher than that for the multiphase model for clarity. The values for the multiphase model are volume fraction averaged plasma and RBC values.

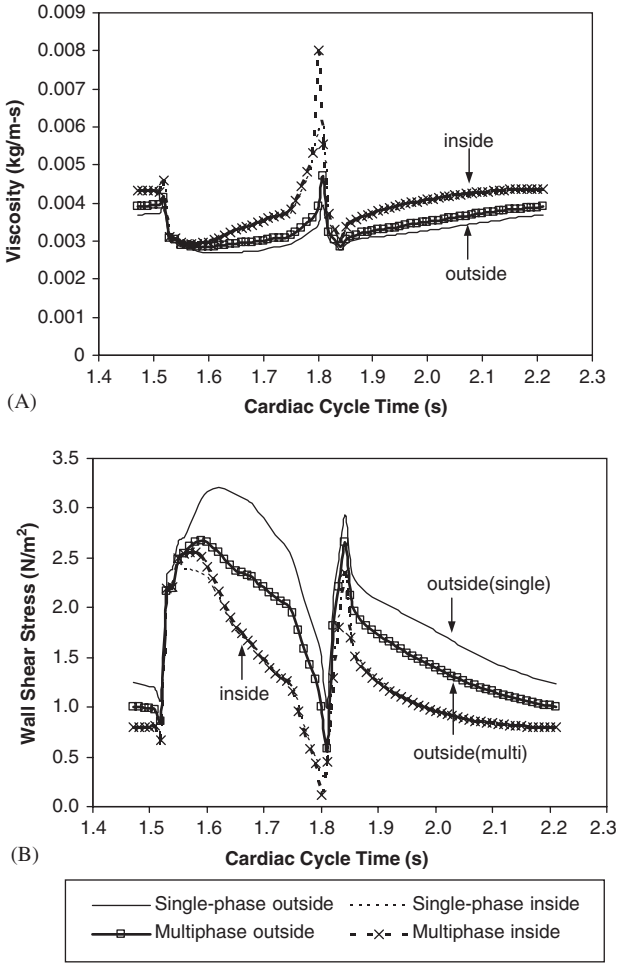

Fig. 9. Comparison of (A) the viscosities and (B) the wall shear stresses for single-phase non-Newtonian model and multiphase non-Newtonian model during the third cardiac systole cycle. The values for the multiphase model are volume fraction averaged plasma and RBC values.

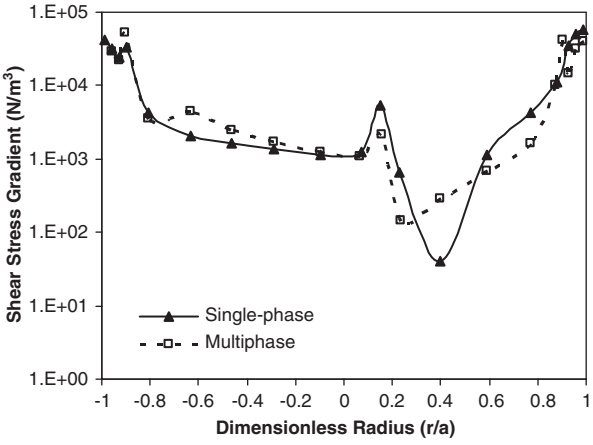

Fig. 10. Comparison of the shear stress gradients for single-phase non-Newtonian model and multiphase non-Newtonian model at the peak of the systole, $t = 1.61$ s. The values for the multiphase model are volume fraction average plasma and RBC values.

correlation between low RBC WSS and RBC buildup on the inside curvature. The multiphase CFD model has also confirmed the well known fact that the RBCs determine the rheological behavior of blood, not possible to prove using the single-phase CFD model. We expect a similar correlation to result for the buildup of blood-borne particulates such as monocytes and platelets which play a role in atherosclerotic plaque formation that usually occurs on the inside curvatures of arteries (Hajjar and Nicholson, 1995; Thubrikar and Robicsek, 1995; Qiu and Tarbell, 2000; Wentzel et al., 2003; Zeng et al., 2003).

Another approach for multiphase flow is the Eulerian–Lagrangian or discrete particle model to analyze monocyte motion under dilute transient conditions in a femoral anastomosis (Longest et al., 2004). In this approach, the plasma and RBCs are treated as a homogeneous non-Newtonian fluid. The RBCs influence on the monocyte trajectories is treated using a dispersion coefficient. The near-wall residence time model was used to compute the deposition rate. This approach is acceptable for dilute flows. Since the number of RBCs is of the order of 10^9 cells/ml, it is impractical to use this approach to model realistically whole blood flow, since the computing time is excessive.

The multiphase Eulerian–Eulerian approach of dense suspension flow describing blood flow has several features. The curvature-induced secondary flow is less dominant in the multiphase non-Newtonian CFD model because of greater shear thinning (Fig. 8). During the cardiac cycle, the secondary flow patterns produced result in the buildup of RBCs on the inside curvature.

The low shear rate in the central region of the curved section produces a high viscosity there because of the shear-thinning behavior. This tends to block the flow of RBCs causing them to migrate preferentially through the boundary layer. The RBC viscosity during the diastole is higher during the systole because of a lower shear rate. The viscosity on the inside curvature wall is higher than that on the outside curvature wall due to higher RBC concentrations The mixture viscosity for multiphase flow agreed with the range of values used for the single-phase simulations performed by Gijsen et al. (1999a) and Berthier et al. (2002), 0.0038 kg/m s (3.8 cp) and 0.004 kg/m s (4.0 cp), respectively.

The WSS trend on the inside and the outside curvatures is in good agreement with results from single-phase CFD model simulations (Qiu and Tarbell, 2000; Zeng et al., 2003). The shear stress is the third term on the RHS of the momentum equations given by Eq. (3). The WSSG is the gradient of the product of the viscosity and shear rate and represents a force per unit volume in the vicinity of the wall. This biomechanical force on the inside curvature of the arterial vessel walls, coupled with low oscillatory WSS may damage and

interact with the endothelium, causing adhesion of monocytes and platelets as described by Stary (1999).

The analysis in this study has considered the dense suspension hemodynamics including RBCs that have previously been ignored in blood flow simulations. We used an idealized uniform circular cross section with rigid walls. The multiphase non-Newtonian CFD model has begun to shed light on important hemodynamic phenomena, such as particulate migration to the surface of endothelial cells, which has eluded investigators using single-phase CFD models. This prediction has possible implications for atherogenesis since it is consistent with clinical observations that atherosclerotic plaque generally forms preferentially in the inside curvatures of coronary arteries.

Acknowledgments

We thank Dr. Horner of Fluent, Inc., for his technical support with the FLUENT code and Professor Shroff of the University of Pittsburgh for his advice in the biomedical area. This study was supported under US Department of Energy Contract W-31-109-Eng-38.

References

Anderson, T.B., Jackson, R., 1967. A fluid mechanical description of fluidized beds. I & EC Fundamentals 6, 524–539.

Berger, S., Jou, L., 2000. Flows in stenotic vessels. Annual Review of Fluid Mechanics 32, 347–382.

Berne, R.M., Levy, M.N., 2001. Cardiovascular Physiology. Mosby, St. Louis.

Berthier, B., Bouzerar, R., Legallais, C., 2002. Blood flow patterns in an anatomically realistic coronary vessel: influence of three different reconstruction methods. Journal of Biomechanics 35, 1347–1356.

Bird, R.B., Armstrong, O., Hassager, R.C., 1987. Dynamics of Polymeric Liquids, second ed. Wiley, New York.

Bonert, M., Leask, R.L., Butany, J., Ethier, C.R., Myers, J.G., Johnston, K.W., Ojha, M., 2003. The relationship between wall shear stress distributions and intimal thickening in the human abdominal aorta. Biomedical Engineering Online 2, I8.

Brooks, D.E., Goodwin, J.W., Seaman, G.V.F., 1970. Interactions among erythrocytes under shear. Journal of Applied Physiology 28, 172–177.

Caro, C.G., Fitz-Gerald, J.M., Schroter, R.C., 1969. Arterial wall shear and distribution of early atheroma in man. Nature 223, 1159–1161.

Cholley, B.P., Shroff, S.G., Sandelski, J., Korcarz, C., Balasia, B.A., Jain, S., Berger, D.S., Murphy, M.B., Marcus, R.H., Lang, R.M., 1995. Differential effects of chronic oral antihypertensive therapies on systemic arterial circulation and ventricular energetics in African-American patients. Circulation 91, 1052–1062.

Davies, P.F., 1995. Flow-mediated endothelial mechanotransduction. Physiological Reviews 75, 519–560.

Davies, P.F., Barbee, K.A., Volin, M.V., Robotewskyj, A., Chen, J., Joseph, L., Griem, M.L., Wernick, M.N., Jacobs, E., Polacek, D.C., DePaola, N., Barakat, A.I., 1997. Spatial relationships in early signaling events of flow-mediated endothelial mechanotransduction. Annual Reviews of Physiology 59, 527–549.

Dill, D.B., Costill, D.L., 1974. Calculation of percentage changes in volumes of blood, plasma, and red cells in dehydration. Journal of Applied Physiology 37, 247–248.

Ding, J., Lyczkowski, R.W., Sha, W.T., Altobelli, S.A., Fukushima, E., 1993. Numerical analysis of liquid–solid suspension velocities and concentrations obtained by NMR imaging. Powder Technology 77, 301–312.

Ding, J., Lyczkowski, R.W., Sha, W.T., 1995. Modeling of concentrated liquid–solids flow in pipes displaying shear-thinning phenomena. Chemical Engineering Communications 138, 145–155.

Fluent, Inc., 2003a. FLUENT 6.1 User's Guide.

Fluent, Inc., 2003b. GAMBIT 2.1 User's Guide.

Fung, Y.C., 1997. Biomechanics: Circulation. Springer, New York.

Gidaspow, D., 1994. Multiphase Flow and Fluidization: Continuum and Kinetic Theory Descriptions. Academic Press, New York.

Gijsen, F.J.H., Allanic, E., Van de Vosse, F.N., Janssen, J.D., 1999a. The influence of the non-Newtonian properties of blood on the flow in large arteries: unsteady flow in a 90° curved tube. Journal of Biomechanics 32, 705–713.

Gijsen, F.J.H., Van de Vosse, F.N., Janssen, J.D., 1999b. The influence of the non-Newtonian properties of blood on the flow in large arteries: steady flow in a carotid bifurcation model. Journal of Biomechanics 32, 601–608.

Hajjar, D.P., Nicholson, A.C., 1995. Atherosclerosis: an understanding of the cellular and molecular basis of the disease promises new approaches for its treatment in the near future. American Scientist 83, 460–467.

Higdon, A., et al., 1976. Mechanics of Materials, third ed. Wiley, New York, pp. 147–157.

Ku, D., 1997. Blood flow in arteries. Annual Review of Fluid Mechanics 29, 399–434.

Lightfoot, E.N., 1974. Transport Phenomena and Living Systems: Biomedical Aspects of Momentum and Mass Transport. Wiley, New York.

Longest, P.W., Kleinstrauer, C., Buchanan, J.R., 2004. Efficient computation of micro-particle dynamics including wall effects. Computers and Fluids 33, 577–601.

Lyczkowski, R.W., Wang, C.S., 1992. Hydrodynamic modeling and analysis of two-phase non-Newtonian coal/water slurries. Powder Technology 69, 285–294.

Malek, A.M., Alper, S.L., Izumo, S., 1999. Hemodynamic shear stress and its role in atherosclerosis. Journal of the American Medical Association 282, 2035–2042.

Nerem, R.M., 1993. Hemodynamics and the vascular endothelium. Journal of Biomechanical Engineering 115, 510–514.

Nichols, W.W., O'Rourke, M.F., 1998. McDonald's Blood Flow in Arteries. Arnold, London.

Poppas, A., Shroff, S.G., Korcarz, C.E., Hibbard, J.U., Berger, D.S., Lindheimer, M.D., Lang, R.M., 1997. Serial assessment of the cardiovascular system in normal pregnancy: role of arterial compliance and pulsatile arterial load. Circulation 95, 2407–2415.

Qiu, Y., Tarbell, J.M., 2000. Numerical simulation of pulsatile flow in a compliant curved tube model of a coronary artery. Journal of Biomechanical Engineering 122, 77–85.

Rappitsch, G., Perktold, K., Pernkopf, E., 1997. Numerical modeling of shear-dependent mass transfer in large arteries. International Journal for Numerical Methods in Fluids 25, 847–857.

Stary, H.C., 1999. Atlas of Atherosclerosis: Progression and Regression. Parthenon Publishing, New York.

Steinman, D.A., 2002. Image-based computational fluid dynamics modeling in realistic arterial geometries. Annals of Biomedical Engineering 30, 482–497.

Steinman, D.A., Vorp, D.A., Ethier, C.B., 2003. Computational modeling of arterial biomechanics: insights into pathogenesis and treatment of vascular disease. Journal of Vascular Surgery 37, 1118–1128.

Stewart, F.C., Lyman, D.J., 2004. Effects of an artery/vascular graft compliance mismatch in protein transport: a numerical model. Annals of Biomedical Engineering 32, 991–1006.

Taylor, C.A., Draney, M.T., 2004. Experimental and computational methods in cardiovascular fluid mechanics. Annual Review of Fluid Mechanics 36, 197–231.

Thubrikar, M.J., Robicsek, F., 1995. Pressure-induced arterial wall stress and atherosclerosis. Annals of Thoracic Surgery 59, 1594–1603.

Wentzel, J.J., Janssen, E., Vos, J., Schuurbiers, J.C.H., Krams, R., Serruys, P.W., de Feyter, P.J., Slager, C.J., 2003. Extension of increased atherosclerotic wall thickness into high shear stress regions is associated with loss of compensatory remodeling. Circulation 108, 17–23.

Wojnarowski, J., 2001. Numerical study of bileaf heart valves performance. In: International Scientific Practical Conference: Efficiency of Engineering Education in XX Century. Donetsk, Ukraine, 29–31 May 2001.

Wootton, D.M., Ku, D.N., 1999. Fluid mechanics of vascular systems, diseases, and thrombosis. Annual Review of Biomedical Engineering 1, 299–329.

Zeng, D., Ding, Z., Friedman, M.H., Ethier, C.R., 2003. Effects of cardiac motion on right coronary artery hemodynamics. Annals of Biomedical Engineering 31, 420–429.